Delft University of Technology

On the influence of sub-pixel position correction for PS localization accuracy and time series quality

Yang, Mengshi; Dheenathayalan, Prabu; Lopez Dekker, Paco; van Leijen, Freek; Liao, Mingsheng; Hanssen, Ramon F.

Citation (APA)
Yang, M., Dheenathayalan, P., Lopez Dekker, P., van Leijen, F., Liao, M., & Hanssen, R. F. (2020). On the influence of sub-pixel position correction for PS localization accuracy and time series quality. *ISPRS Journal of Photogrammetry and Remote Sensing*, *165*, 98-107. https://doi.org/10.1016/j.isprsjprs.2020.04.023
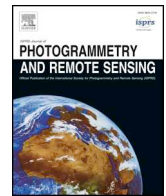
Important note
To cite this publication, please use the final published version (if applicable).
Please check the document version above.

On the influence of sub-pixel position correction for PS localization accuracy and time series quality

Mengshi Yang[a,b], Prabu Dheenathayalan[b], Paco López-Dekker[b], Freek van Leijen[b], Mingsheng Liao[a,*], Ramon F. Hanssen[b]

[a] *State Key Lab. of Information Engineering in Surveying, Mapping and Remote Sensing, Wuhan University, Wuhan 430079, China*
[b] *Department of Geoscience and Remote Sensing, Delft University of Technology, 2628CN Delft, the Netherlands*

ARTICLE INFO

ABSTRACT

Persistent Scatterer Interferometry (PSI) is a time series remote sensing technique to estimate displacements of geo-objects from the interferometric phases of selected Persistent Scatterers (PS). The relative position of a scatterer within a resolution cell causes an additional phase contribution in the observed phase, which needs to be accounted for in PSI processing. Here we analyze the influence of this sub-pixel position correction on point localization and displacement quality. Apart from a theoretical evaluation, we perform experiments with TerraSAR-X, Radarsat-2, and Sentinel-1, demonstrating various levels of improvement. We show that the influence of the sub-pixel correction is significant for the geolocation of the scatterer (meter-level improvement), modest for the elevation estimation (centimeter-level improvement), and limited for the displacement estimation (submillimeter-level). For displacement velocities, we find variations of a few tenths of a millimeter per year. The effect of sub-pixel correction is most dominant for large orbital baselines and short time series.

1. Introduction

Synthetic Aperture Radar Interferometry(InSAR), in particular the family of techniques developed to analyze interferometric time series (stacks), has evolved into a geodetic tool for mapping the topography or displacement of the Earth's surface or objects on it. One of the most successful approaches is Persistent Scatterer Interferometry (PSI), in which the phase of pixels corresponding to coherent scatterers over time is exploited (Ferretti et al., 2001; Crosetto et al., 2016). InSAR processing typically attempts to remove all phase contributions that can be predicted, such as the phase contribution due to the ellipsoidal shape of the Earth and the topographic phase (Hanssen, 2001). These phase terms are range and azimuth dependent and are typically calculated for the nominal center position of each pixel. Yet, for point-like targets, the position of a dominant scatter does not necessarily coincide with the center position of the pixel. As a result, the phase of those targets receives a biased correction.

In this study, the phase contribution due to the sub-pixel position of a dominant scatterer is referred to as the sub-pixel phase. Clearly, the better we can perform the phase correction, the more accurate the estimated parameters will be. Correcting the sub-pixel phase has been

suggested by Kampes (2006). Hooper (2006) showed that the phase due to the range position of a dominant scatterer is especially important for height estimation when only a few (<12) interferograms are available. Using corner reflectors, Marinkovic et al. (2004, 2008) reported errors of 3.8 and 0.7 mm in displacement phase observations for ERS-2 and Envisat, respectively. However, currently there is no systematic analysis of the generic impact and significance of the sub-pixel position on the final PSI results, specifically considering the consequences for the precision of PS localization and the quality of the estimated displacements.

We assess the influence of the sub-pixel position on PSI positioning and displacement estimates, and evaluate the conditions under which a sub-pixel correction needs to be applied. A method is presented to find the exact phase center of the dominant scattering object within the resolution cell and to mitigate the influence of residual scattering elements. The impact of sub-pixel correction is discussed by comparing the results of PSI with and without sub-pixel correction.

In Section 2, we investigate the effect of the sub-pixel phase on PSI results. PSI with sub-pixel correction has been implemented for evaluating its influences in Section 3. The analysis has been tested on stacks of TerraSAR-X, Radarsat-2, and Sentinel-1 images as described in Section 4. Sections 5 discusses the effects on displacement estimation and
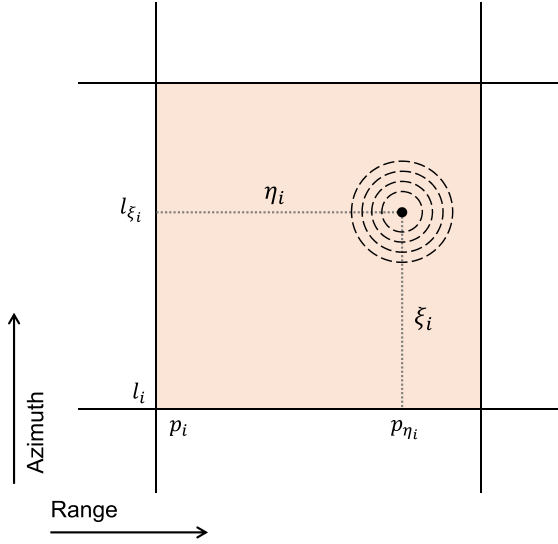

Fig. 1. The effective scattering center within a image pixel is shifted ξ_i in azimuth and η_i in range from the near-range, early azimuth corner (l_i, p_i).

topography estimation. Section 6 provides the conclusions of this study.

2. Sub-pixel phase and its influence on PSI results

The observed phase ϕ_i^{ms} of pixel i in an interferogram from SAR images m and s is composed of:

$$\phi_i^{ms} = -2\pi a + \phi_{i,\text{ref}} + \phi_{i,\text{topo}} + \phi_{i,\text{disp}} + \phi_{i,\text{atmo}} + \phi_{i,\text{noise}}, \quad (1)$$

where a is the integer phase ambiguity, $\phi_{i,\text{ref}}$ is the reference phase corresponding to the ellipsoid, $\phi_{i,\text{topo}}$ is the topographic phase, $\phi_{i,\text{disp}}$ is the displacement phase, $\phi_{i,\text{atmo}}$ is the atmospheric phase, and $\phi_{i,\text{noise}}$ is the noise term.

The reference phase is calculated with an ellipsoid model and the topographic phase is calculated with an external DEM. Typically, both components are evaluated at the early-azimuth, near range corner of the pixel. However, the effective phase center can be situated at any arbitrary position ξ_i in azimuth and η_i in ground-range from the corner (l_i, p_i), see Fig. 1. Thus, the components $\phi_{i,\text{topo}}^{l_i,p_i}$ and $\phi_{i,\text{ref}}^{l_i,p_i}$ omit the contribution due to the sub-pixel position within the pixel, resulting in a phase bias $\phi_{i,\text{sub}}$,

$$\phi_i^{ms} - \phi_{i,\text{ref}}^{l_i,p_i} - \phi_{i,\text{topo}}^{l_i,p_i} = -2\pi a + \phi_{i,\text{disp}} + \phi_{i,\text{atmo}} + \phi_{i,\text{noise}} + \phi_{i,\text{sub}}. \quad (2)$$

2.1. Sub-pixel position phase

The sub-pixel phase is due to the uncompensated reference and topographic phase. The sub-pixel phase can be written as

$$\phi_{i,\text{sub}} = \phi_{i,\xi} + \phi_{i,\eta} + \phi_{i,\Delta h_i}, \quad (3)$$

where $\phi_{i,\xi}$ and $\phi_{i,\eta}$ are the uncompensated reference phases dependent on the azimuth ξ_i and ground-range η_i sub-pixel position, and $\phi_{i,\Delta h_i}$ is the uncompensated DEM phase due to the elevation difference Δh_i between (l_{ξ_i}, p_{η_i}) and (l_i, p_i). These terms will be discussed subsequently.
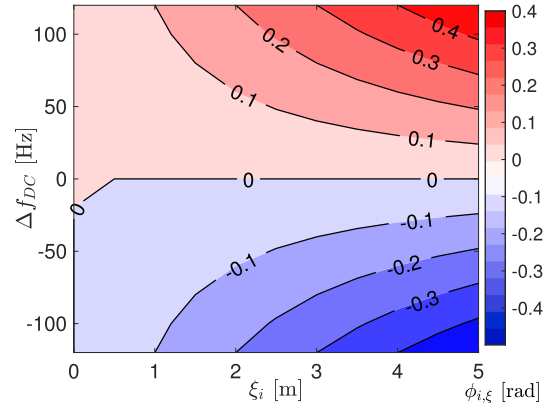
Azimuth. Using the far-field approximation (Zebker and Goldstein, 1986; Hanssen, 2001), the azimuth phase term is given as (Kampes, 2006)

$$\phi_{i,\xi} = \frac{-4\pi}{\lambda} \cdot (\sin\vartheta^m - \sin\vartheta^s) \cdot \xi_i, \quad (4)$$

where λ is the wavelength, and ϑ^m and ϑ^s are the squint angles of the master and slave image, respectively. Fig. 2(a) illustrates the geometry for the additional phase due to the azimuth sub-pixel position ξ_i. Given
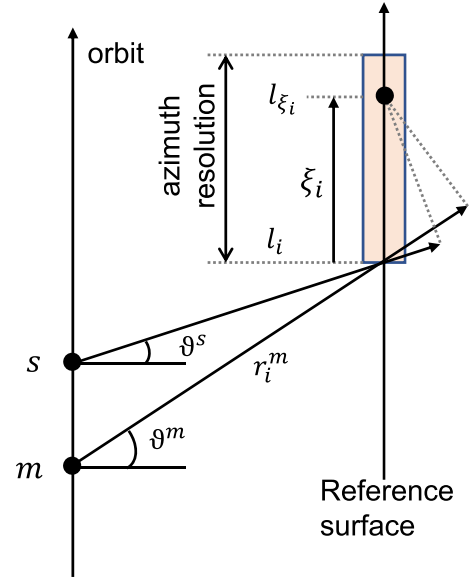
(a)

(b)

Fig. 2. (a) Phase term due to the azimuth sub-pixel position ξ_i. The signal path length changes because of the variation in squint angle ϑ, resulting in a phase term $\phi_{i,\xi}$. Adapted from Marinkovic et al. (2004). (b) Sub-pixel phase term in azimuth as a function of the dominant scatterer location and Δf_{DC} in case of Radarsat-2.

the relation between the squint angle and the Doppler centroid frequency (Bamler and Schättler, 1993),

$$f_{\text{DC}} = \frac{-2\upsilon}{\lambda} \cdot \sin\vartheta, \quad (5)$$

where f_{DC} is the Doppler centroid frequency and υ is the velocity of the satellite, (4) can be rewritten as (Kampes, 2006)

$$\phi_{i,\xi} = \frac{2\pi}{\upsilon} \cdot (f_{\text{DC}}^m - f_{\text{DC}}^s) \cdot \xi_i. \quad (6)$$

Hence, the azimuth sub-pixel phase term is related to the difference in the Doppler centroid frequencies. If there were a linear drift in the Doppler centroid, this signal would cause an apparent constant displacement rate. Fig. 2(b) shows the azimuth phase term as a function of scatterer sub-pixel position in azimuth and differences in Doppler centroid values $\Delta f_{\text{DC}} = f_{\text{DC}}^m - f_{\text{DC}}^s$, in case of Radarsat-2 ($\lambda = 5.6$ cm, $\theta = 35°$, $\upsilon = 7550$ m/s). The horizontal axis shows the sub-pixel position in azimuth within a resolution cell ξ_i. The vertical axis shows the differences in Doppler centroid values Δf_{DC}. The azimuth sub-pixel phase

(a)

(b)

Fig. 3. (a) Phase term due to the ground-range sub-pixel position η_i. The signal path length changes because of the variation in incidence angle θ, resulting in a phase term $\phi_{i,\eta}$. Adapted from Marinkovic et al. (2004). (b) Sub-pixel phase term in range as a function of the dominant scatterer location and $B_\perp$ in case of Radarsat-2.
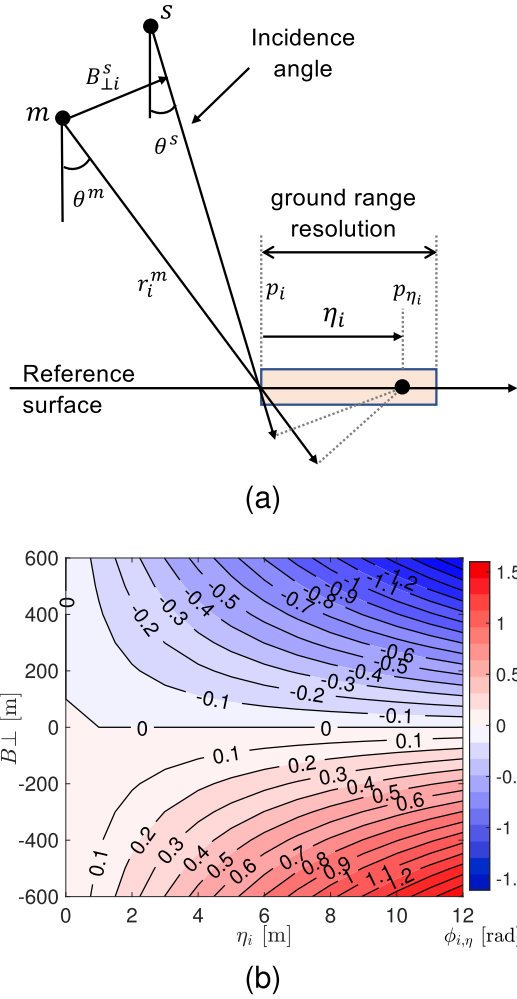
term is calculated with ξ_i and Δf_{DC} as (6), and indicated with the color. The phase term is proportional to increasing values of ξ_i and Δf_{DC}. If $\xi_i = 4.9$ m, the sub-pixel phase shift is 4 mrad/Hz (0.2°/Hz) per Hz Doppler centroid difference.

Range. The ground-range sub-pixel phase term is (Kampes, 2006)

$$\phi_{i,\eta} = \frac{-4\pi}{\lambda} \cdot (\sin\theta^m - \sin\theta^s) \cdot \eta_i, \tag{7}$$

where θ^m and θ^s are the incidence angles of master and slave. The phase term can be rewritten using $\theta^m - \theta^s \approx B_\perp / r_i^m$ as

$$\phi_{i,\eta} = \frac{4\pi}{\lambda} \cdot \frac{B_\perp}{r_i^m} \cdot \cos\theta^m \cdot \eta_i, \tag{8}$$

where $B_\perp$ is the perpendicular baseline between master and slave, and r_i^m is the range to the master antenna.

The ground-range sub-pixel phase term is equal to the reference phase variation due to the incidence angle under the far field approximation, see A. Fig. 3(a) shows the phase term due to the ground-range sub-pixel position. Fig. 3(b) gives the range phase in case of Radarsat-2 data as a function of scatterer position and perpendicular baseline. The horizontal axis is the sub-pixel position in ground range within a resolution cell η_i. The vertical axis is the perpendicular baseline values of $B_\perp$. The phase term is calculated with η_i and $B_\perp$ as (8), and plotted in color. The phase term is proportional to increasing values of η_i and $B_\perp$. If

$\eta_i = 11.8$ m, a $B_\perp$ of 100 m will cause $- 0.26$ rad ($- 15°$) phase shift.

Elevation. The residual height term is

$$\phi_{i,\Delta h_i} = \frac{-4\pi}{\lambda} \cdot \frac{B_\perp}{r_i^m \sin\theta^m} \cdot \Delta h_i. \tag{9}$$

This term depends on the difference Δh_i between the DEM-height for the early-azimuth, near-range pixel corner and the DEM-height for the position of the scatterer. However, as standard PSI processing already includes the estimation of 'DEM-errors', relative to the reference DEM, the influence of the sub-pixel height is already compensated for.

2.2. Influence on geolocation accuracy

In the slant-range and azimuth radar coordinate system, the location of a scatterer can be anywhere within the pixel. Thus, the maximum deviation (or absolute error) of a scatterer is equal to the pixel size, both in range and azimuth direction. For Sentinel-1 IW data with an incidence angle of 37 degrees, e.g. the geolocation error can be up to 4 m in ground-range and 14 m in azimuth.

However, in the zero-Doppler plane, the geolocation error is not only dependent on the sub-pixel position η_i in the ground-range but also on the vertical position within the range bin. The vertical position is described by the height difference relative to a reference height and is estimated from phase observation. The position of a target is determined by combining range distance and phase using Range-Doppler-Ellipsoid/DEM equations (Schreier, 1993).

As described in Section 2.1, InSAR removes the phase components that can be predicted. Fig. 4 shows a range bin in the zero-Doppler plane, where a height error is caused by uncompensated reference phase. A point target within this range bin would be aligned to the near-range side of the pixel, i.e., line 1. If the height of the target is zero, the point is located at T_1. Estimating the sub-pixel position by oversampling the data yields a slant-range shift of p_{η_i}. This implies that line 1 is translated to line 2, which changes the horizontal position to T_2. Thus, the reference phase component should be evaluated at position T_2. If the reference phase is calculated at the near-range side of the pixel (T_1) then part of the reference phase is not removed, i.e., the reference phase difference between the two positions.

The residual reference phase is (Hanssen, 2001)

$$\Delta\phi_{12,\text{ref}} = \frac{4\pi}{\lambda} \cdot B_\perp \cdot \theta_{12}, \tag{10}$$

where θ_{12} is the incidence angle difference between position T_1 and T_2. The reference phase is linearly depend on the perpendicular baseline $B_\perp$.
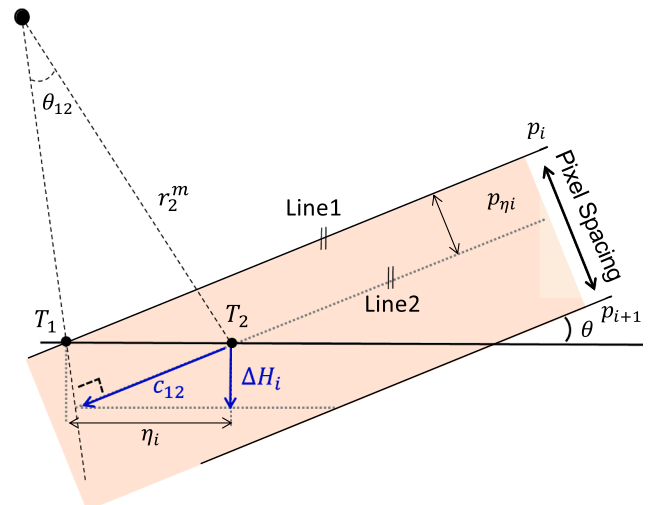
Fig. 4. The uncompensated reference phase at the near-range side of the pixel T_1 causes a height error ΔH_i.
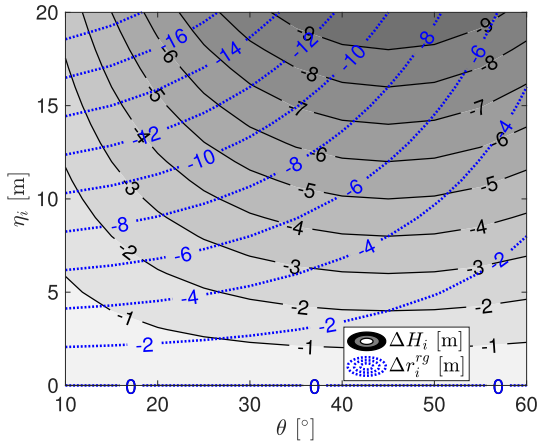
Fig. 5. Height error ΔH_i and ground range error Δr_i^{rg} as function of range sub-pixel position η_i and incidence angle θ, in the case of Radarsat-2 data.

Fig. 6. Influence of the sub-pixel position of a dominant scatterer in the zero-Doppler plane on geo-localisation. Without sub-pixel correction, the true position, T_i, is georeferenced to position T_1. Applying sub-pixel correction, the location shifts to position T_i.

In PSI analysis, this phase component would typically be adsorbed by the topographic phase estimation. Hence, the residual reference phase results in a height error

$$\Delta H_i = -\sin\theta^m r_i^m \theta_{12}. \tag{11}$$

Since the cross-range distance c_{12} between T_1 and T_2 is

$$c_{12} \approx r_i^m \theta_{12} = \eta_i \cos\theta^m, \tag{12}$$

see Fig. 4, the height error thus be then written as (van Leijen, 2014)

$$\Delta H_i = -\eta_i \sin\theta_m \cos\theta^m. \tag{13}$$

Fig. 5 illustrates this height error ΔH_i as a function of the sub-pixel location and the incidence angle, in the case of Radarsat-2 data. For a ground range spacing of about 21 m, and a local incidence angle of 34°, this will cause a height error of -9.8 m.

The relation between the horizontal shift (ground range distance) and the height error is

$$\Delta r_i^{\mathrm{rg}} = \frac{\Delta H_i}{\tan\theta^m}. \tag{14}$$

Combining (13) and (14), the subsequent error in ground-range is given by (van Leijen, 2014)

$$\Delta r_i^{\mathrm{rg}} = -\eta_i \cos^2\theta^m. \tag{15}$$

We visualized the ground-range error as a function of the incidence angle and the sub-pixel location in Fig. 5. The errors decrease for increasing incidence angles in a side looking system, similar to the effect of foreshortening.

Therefore, without sub-pixel correction, the geolocation error is a combination of the sub-pixel position p_{η_i} and the ΔH_i due to the residual reference phase. In Fig. 6, depicting a range bin in the zero-Doppler plane, a point target at T_i would by default be considered to be located at the near-range side of the pixel along the line 1. Considering the ellipsoid as a reference, the scatterer would be positioned at location T_1 with height H_i. After correcting the sub-pixel position p_{η_i} and the ΔH_i due to the residual reference phase, the location shifts to position T_i.

2.3. Influence on displacement estimation

Several deformation models can be used for estimating deformation in PSI processing. The simplest one is the steady-state (constant velocity) linear displacement model (Ferretti et al., 2001; Crosetto et al., 2016). Assuming a steady-state model, any temporal drift in Δf_{DC}, in combination with an azimuth sub-pixel position error, can be mis-interpreted as a bias in the displacement velocity estimate. Range sub-pixel positions in combination with any distribution of perpendicular baselines will result in a height estimation error.
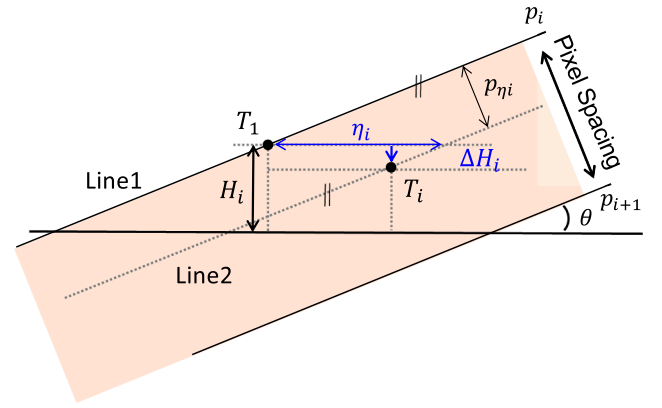
In most cases, in particular when the time-series are long enough, the Doppler offsets seem to be independent of time. Thus, even without the sub-pixel correction, the corresponding phase term is not likely to affect the final displacement velocity estimates. However, if a temporal drift in Δf_{DC} cannot be excluded, applying the correction would improve the displacement velocity estimate.

Aside from correcting systematic phase terms, sub-pixel processing will generally result in an improved amplitude estimation, hence a better signal-to-clutter ratio, as values are closer to the true position of the dominant target.

A non-zero sub-pixel position, in combination with DEM errors and time-dependent variation in the perpendicular baseline or Doppler centroid frequency will affect the observed phase values. Consequently, it is difficult to estimate the sub-pixel phase component directly from the observed phase. As an alternative, we can estimate the sub-pixel position of the dominant scatterer from the amplitude data, and subsequently apply the corresponding phase correction.

3. Methodology

As it is not feasible to estimate the sub-pixel phase term directly from the phase observations, we localize the position of the dominant scatterer based on amplitude information and subsequently correct the phase term related to the sub-pixel position in the interferometric phase. In the following, this processing method is referred to as sub-pixel PSI (SP-PSI).

3.1. Dominant scatterer localization

Here we estimate the sub-pixel location straightforwardly by up-sampling the single-look-complex data in a small region around each scatterer and determining the position of the intensity-peak. This up-sampling can be done in several ways (Keys, 1981; Parker et al., 1983; Quegan, 1990; Hanssen and Bamler, 1999; Perissin, 2006; Shi et al., 2015; Zhang and López-Dekker, 2019). In our case we use a sinc-interpolation (Cumming and Wong, 2005; Gonzalez and Woods, 2007) which is implemented efficiently in the frequency domain. This implies a Discrete Fourier Transform (DFT) of the block, a zero padding operation, and an inverse DFT. Fig. 7 visualizes the procedure. The input is the data block around pixel (l_i, p_i). The effective scattering phase center (l_{ξ_i}, p_{η_i}) is detected by finding the maximum peak of the interpolated signal.

The variance of estimated peak position i in azimuth $\sigma_{l,i}^2$ and range $\sigma_{p,i}^2$ direction is given by (Bamler and Eineder, 2005)
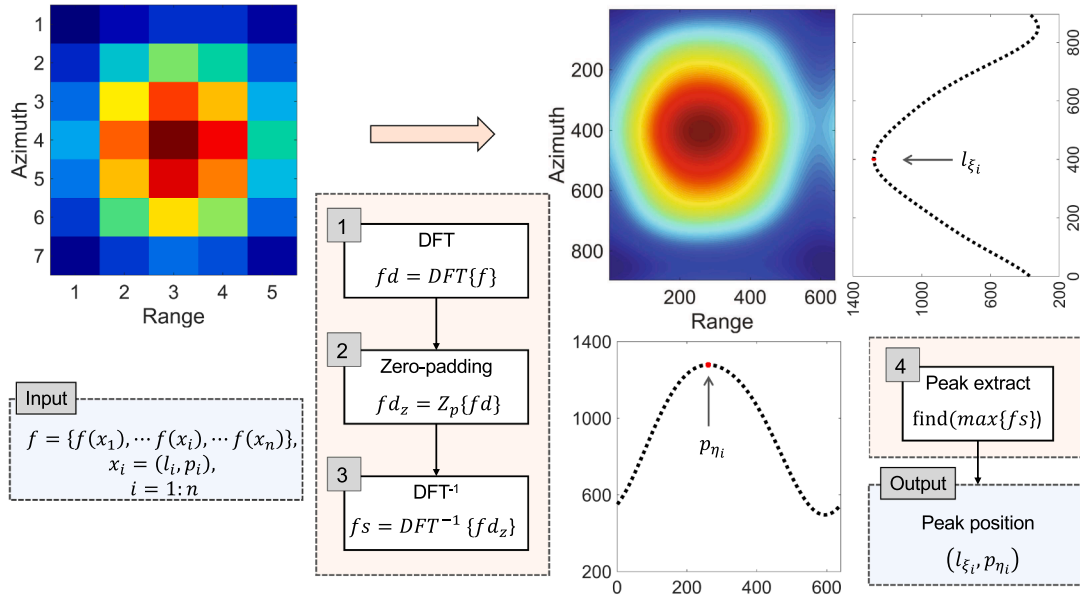
Fig. 7. Position of the dominant scatterer detected based on amplitude information by FFT oversampling. Left: original amplitude image. Right: the oversampled image. The effective scattering center is found at the local maximum.

$$\sigma_{l,i}^2 = \sigma_{p,i}^2 = \frac{3}{2 \cdot \pi^2 \cdot \text{SCR}_i}, \tag{16}$$

where SCR is the signal-to-clutter ratio of a point. (16) is the Cramér-Rao bound for a change of the peak due to clutter (Stein, 1981; Bamler and Eineder, 2005), under the assumption of a homogeneous area and circularly Gaussian clutter. After determining the sub-pixel position of the dominant scatterer, the corresponding reference phases are computed and compensated.

3.2. Sub-pixel correction processing chain

To analyze the influence of the sub-pixel correction, a sub-pixel correction module is designed and embedded in the Delft Persistent Scatterer Interferometry (DePSI) toolbox (Kampes, 2006; van Leijen, 2014), see Fig. 8. It includes localizing the sub-pixel position of the scattering center and correcting the corresponding phase terms ϕ_i^{ms}.

PS Candidates (PSC) are selected based on their normalized amplitude dispersion. The sub-pixel correction is performed for each selected $\text{PSC}(l_i, p_i)$, where $i = 1 : M$, and M is the number of PSCs. For each PSC, we use an $n \times n$ complex data block centered at the PSC position and estimate the peak position and the corrected phase ϕ_i^{ms}. After determining the sub-pixel position, (3) is applied to determine the phase

Fig. 8. Processing chart of PSI including the sub-pixel correction module, as implemented in DePSI.

correction term, which is subtracted from the phase of the original PSC.

After the sub-pixel correction a standard PSI processing flow is applied, including network construction, spatio-temporal (3D) phase unwrapping, atmospheric phase mitigation, final PS selection, and geocoding. The results presented were obtained using DePSI (Kampes, 2006; van Leijen, 2014). In-depth discussions of PSI processing can be found in Ferretti et al. (2001), Hooper (2006), Kampes (2006), van Leijen (2014), Crosetto et al. (2016).

The steps of network construction, phase unwrapping, and atmosphere mitigation were executed iteratively after PS selection. The PS were re-selected based on the deviation of the unwrapped phase time-series of each PS from a pre-defined deformation model. When the standard deviation of the residual phase of the PS exceeds a certain threshold, the PS is discarded because the corresponding estimation is assumed to be unreliable. It is worth pointing out that this procedure will also eliminate high quality PS that do not follow the selected model (Chang and Hanssen, 2016). As this is not a SP-PSI specific issue, the comparison of performances remains valid. Here, we set the number of iterations to five.

4. Experiment setting

In order to analyze the influence of sub-pixel correction on PSI results, we analyzed three data stacks with different resolutions, acquired by TerraSAR-X, Radarsat-2, and Sentinel-1. For our analysis we consider an area around Delft, the Netherlands.

Fig. 9 shows the location of the test area, the bounding polygons of the data stacks, and the location of the installed reflectors. The relevant parameters of the data stacks are provided in Table 1. The perpendicular baselines and Doppler centroid differences have a considerably larger spread in the Radarsat-2 case. Meanwhile, there is a relatively long time series of Radarsat-2 data, covering about five years.

Seven reflectors, CR1–CR7, were installed at the Ypenburg test site between August 2012 and March 2014 with an orientation optimized for the TerraSAR-X acquisitions. Fig. 10(a) shows those reflectors in the mean intensity image of 46 TerraSAR-X images. We use CR4‘7 in our analysis to avoid the impact of the mutual side-lobes of the first three.

For our analysis of the Sentinel-1 stack, we used two reflectors installed at the Wassenaar test site since November 2017, see Fig. 10(b). Differential GPS and tachymetry are used to precisely determine the
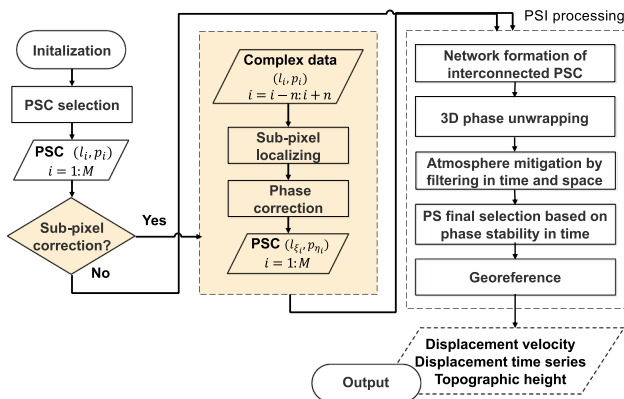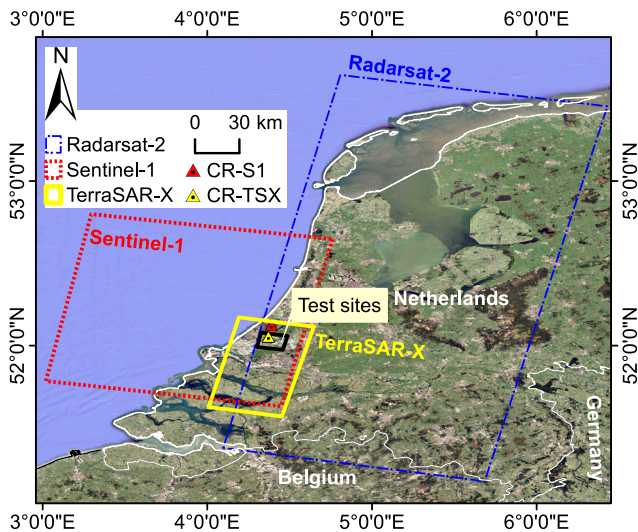
Fig. 9. The coverage of TerraSAR-X, Radarsat-2, and Sentinel-1 data. Triangles indicate the location of corner reflectors installed for TerraSAR-X and Sentinel-1.

Table 1
TerraSAR-X, Radarsat-2, and Sentinel-1 SAR Data characteristics.

Mission/Parameter	TerraSAR-X	Radarsat-2	Sentinel-1
Track	T048	T202	T110
Band	X	C	C
Start Date	2012.08.11	2010.06.20	2017.11.08
End Date	2014.03.06	2015.02.18	2018.07.18
Number of images	46	64	40
$B_\perp$ [min/max] [m]	−382/142	−576/317.7	−88.4/117.7
Δf_{DC} [min/max] [Hz]	−78.9/70.8	−103.2/122.8	−17.7/73.3
Acquisition mode	Stripmap	Standard	Interferometric Wide
Pass direction	Descending	Descending	Descending
Polarization	HH	HH	VV
Incidence angle [°]	22.3–25.6	30.6–37.1	35.7–41.7
Heading [°]	192.2	191	190
Range sampling [m]	0.9	11.8	2.3
Azimuth sampling [m]	1.7	4.9	13.8
Range Bandw. [MHz]	150	11.6	56.5
Azimuth Bandw. [Hz]	2765	900	327

apex positions of these CRs. These positions are determined with a precision of 1 cm (1σ) in the horizontal dimensions (East and North), and 2 cm in the vertical direction.

5. Results

The analysis was performed by comparing linear velocity estimates and displacement time series, and the 3D geolocation precision between PSI and SP-PSI.

5.1. Displacement estimation

Fig. 11(a) shows the estimated displacement velocities for the PS identified in the TerraSAR-X data stack by SP-PSI, i.e., PSI with sub-pixel correction. Fig. 11(b) shows the velocity differences between PSI and SP-PSI. Similarly, the estimated velocities and the velocity differences of Radarsat-2 and Sentinel-1 data stacks are given in Figs. 12 and 13, respectively.

Very similar displacement signals are observed in the three stacks, despite the fact that the stacks cover different time spans. This indicates that the majority of the points follow a constant displacement (subsidence) velocity sustained in time.

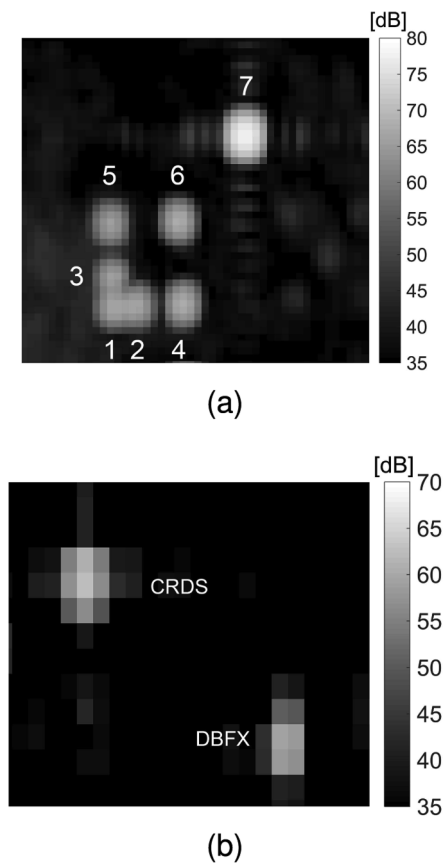Fig. 14 shows the histograms of the differences in estimated

(a)

(b)

Fig. 10. (a) Mean intensity image from 46 TerraSAR-X images covering the seven corner reflectors, (b) Mean intensity image from 40 Sentinel-1 images covering the two reflectors.

velocities. Compared to TerraSAR-X and Radarsat-2, a larger spread of velocity differences was observed in the case of Sentinel-1, which can be explained by the shorter time series of Sentinel-1, which results in more influence of noise.

To further evaluate the results by PSI and SP-PSI, three indicators were used, see Table 2: the number of accepted points (NP) after final selection; the standard deviation, σ_D, of the residuals between the displacement model and the displacement time series, and the Spatio-Temporal Consistency (STC), which expresses the minimum root mean square error of the double-differences between PS and various surrounding PS (van Leijen, 2014).

Table 2 reveals that the number of points improved by applying the sub-pixel correction, most notably for Sentinel-1, yielding 5% more points. All PS candidates were re-selected by evaluating the deviation of unwrapped time series from the deformation model, as introduced in Section 3. In this step, more points were preserved in the PSI results with sub-pixel correction. Applying sub-pixel correction relieves the phase terms related to Doppler offsets from the interferometric phase. The increasing number of points reflects the reduced phase noise with the sub-pixel correction. While the σ_D and STC improved slightly by applying the sub-pixel correction, all metrics show a consistent improvement after sub-pixel correction.

To clearly show the differences in time series displacement between PSI and SP-PSI results, we plotted displacement differences of 500 arbitrary PS per epoch in Fig. 15, together with the perpendicular baselines and Doppler centroid differences of the three stacks. The differences in displacements per epoch ranged between −1 and 1 mm. For TerraSAR-X, almost no differences are observed between the results by PSI and SP-PSI. In the case of Radarsat-2, the largest differences were observed at epochs with a relatively long baseline. The displacement
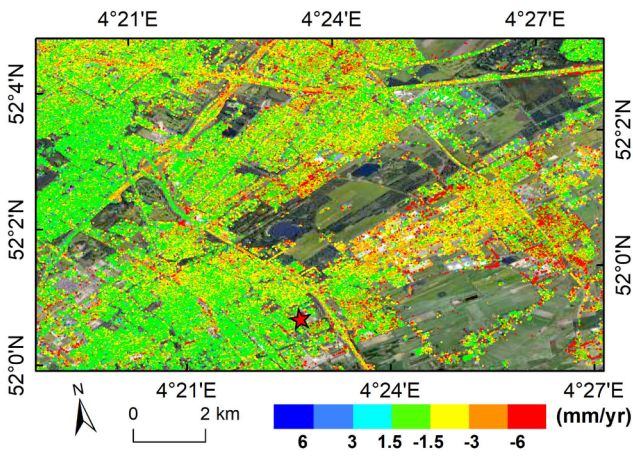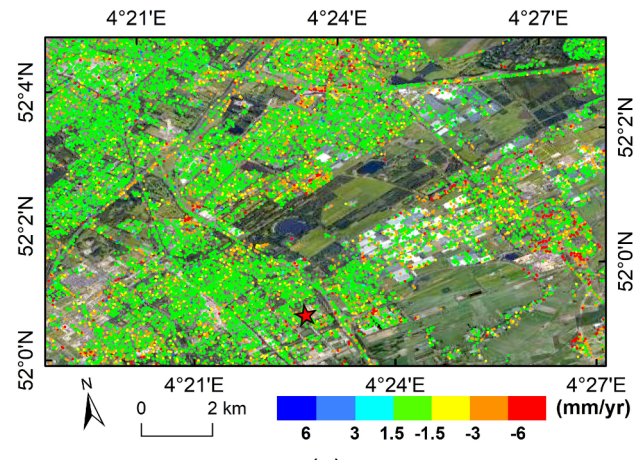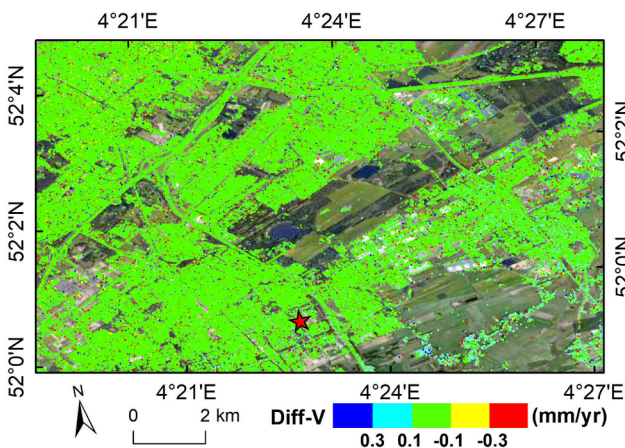
Fig. 11. (a) Estimated linear velocities by SP-PSI for the TerraSAR-X stack. The reference point is indicate by the red star. (b) Differences in the estimated velocity between SP-PSI and PSI.

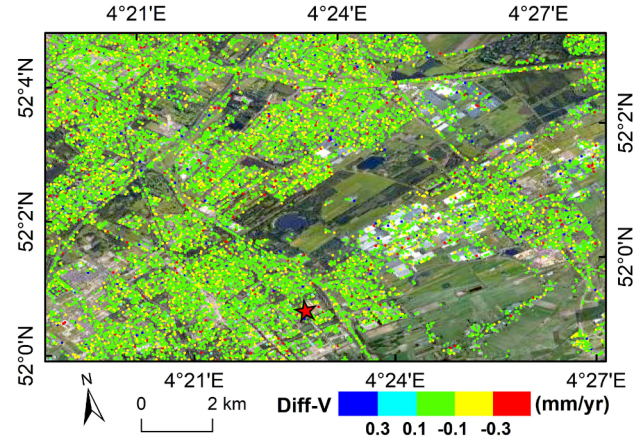**Fig. 12.** (a) Estimated linear velocities by SP-PSI for the Radarsat-2 stack. The reference point is indicate by the red star. (b) Differences in the estimated velocity between SP-PSI and PSI.

differences of Sentinel-1 are random showing no relation with the baselines or the Doppler offsets.

5.2. Geolocation precision

The PS point cloud was projected in the Dutch national reference system RD and vertical reference system NAP. The coordinate differences at all points measured by PSI and SP-PSI are summarized in Table 3.

As expected, the smallest average differences are observed for TerraSAR-X due to its fine resolution. The vertical differences correspond to the residual reference phase as discussed in Section 2.2, which is linear dependent on $B_\perp$. As the baseline of the Sentinel-1 stack is relatively shorter due to its constrained small orbital tube, the influence on the reference phase is small, and the standard deviation of vertical differences for Sentinel-1 are the smallest. Conversely, the largest differences were observed for Radarsat-2, which results in large shifts within the resolution cell and a larger height component due to the wide range of baselines.

The 3D positioning accuracy is further evaluated with the installed reflectors. The calculated positioning result by PSI is the relative measurement, as the cross-range distance of each PS in radar geometry is estimated from the interferometric pairs relative to a reference point (Yang et al., 2019). Hence, the 3D point position of the reflectors

calculated by PSI cannot be directly verified with the position measured by GNSS. The double-difference coordinates were used for the evaluation to avoid deviations from the reference point. The verification results show the relative positioning accuracy of PSI and the accuracy of distance measurements. Using CR6 as the reference, we calculated the double-difference coordinates measured by PSI, SP-PSI, and GPS. Fig. 16 graphically compares the locations of CR4, CR5, and CR7 relative to CR6, by SP-PSI, and PSI, to the apex locations estimated by GPS. The Root Mean Square Error (RMSE) of the double-differences coordinates relative to GPS positions are given in Table 4.

There are distinct improvements in the cross-range direction, with a decreasing the RMSE of InSAR-GPS from 4.00 m to 1.22 m with subpixel correction. As the TerraSAR-X data have a fine resolution, the improvement is small both in azimuth and range directions, about 0.2 m. In local coordinates, the improvement in cross-range not only converts to up-direction, but also to east and north directions. Fig. 16 demonstrates that the positions estimated by SP-PSI are closer to the actual(GPS) locations.

The evaluation of PS measured by Sentinel-1 is given in Table 5. The RMSE in the azimuth direction has improved clearly due to the poorer azimuth resolution. This improvement propagates to the north direction. The improvement in cross-range is smaller than in the TerraSAR-X result, which is a result of the smaller range of cross-track baselines.
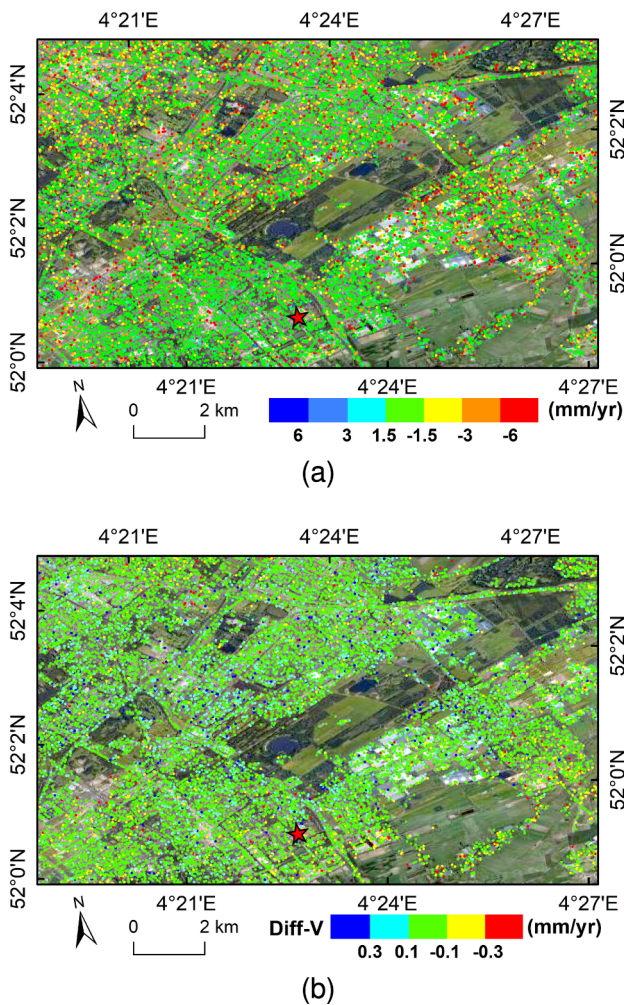
Fig. 13. (a) Estimated linear velocities by SP-PSI for the Sentinel-1 stack. The reference point is indicate by the red star. (b) Differences in the estimated velocity between SP-PSI and PSI.

5.3. Necessity

This section provides a reference for assessing the necessity of sub-pixel correction. Sub-pixel correction is applicable to point-like targets,

Table 2
Quality indicators of TerraSAR-X, Radarsat-2, and Sentinel-1 data-stacks results by PSI and PS-PSI.

		NP	σ_D [mm] mean	STC [mm] mean
TSX	PSI	288,287	0.27	1.81
	SP-PSI	290,768	0.26	1.80
RS2	PSI	51,041	0.53	3.70
	SP-PSI	51,436	0.53	3.67
S1	PSI	52,261	2.68	2.69
	SP-PSI	54,819	2.54	2.68

whose position is well defined. It is not relevant in the case of distributed scatterers. The sub-pixel correction is often neglected in PSI processing aimed at displacement applications. As presented in this study, the improvement in estimated velocities is marginal (the differences are smaller than 1 mm/y). Yet, the sub-pixel correction does enable more points to be selected.

For the positioning of the selected persistent scatterers, the improvement is significant and more relevant. The precise point positioning of individual scatterers needs the sub-pixel correction (Gernhardt et al., 2015; Yang et al., 2019). Moreover, in applications relying on the precise positioning of individual scatterers sub-pixel correction should be applied. The consequences of sub-pixel correction are summarized in Table 6.

6. Conclusions

This study analyzes the influence of relative position of a scatterer within a resolution cell on PSI results.

In theory, as long as baselines and Doppler offsets do not show a temporal trend, neglecting the sub-pixel correction should not impact the estimated velocities and displacements significantly. Conversely, any systematic trend in the baseline or the Doppler centroid will introduce a proportional trend in the displacement signal.

Working at the sub-pixel level results in a reduced phase noise, which in turn leads to an increased number of selected points. In the case of Sentinel-1, a 4% increase in the number of points was obtained.

The main improvement resulting from sub-pixel PSI processing is the improved positioning of persistent scatterers. The largest differences were observed in the Radarsat-2 results, which is explained by the relatively low resolution and considerable baseline dispersion. GPS measurements have validated the improvements using sub-pixel correction, which yields a maximum improvement for the TerraSAR-X
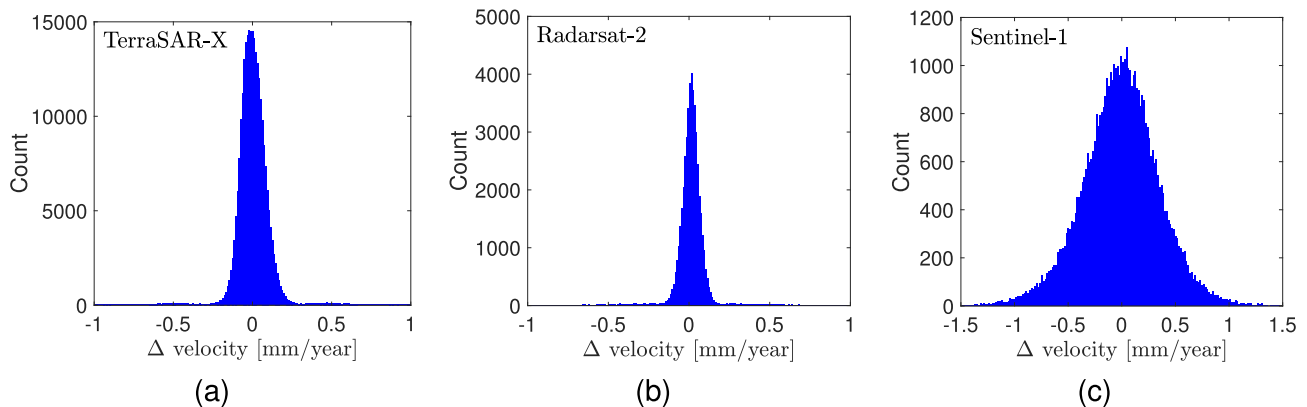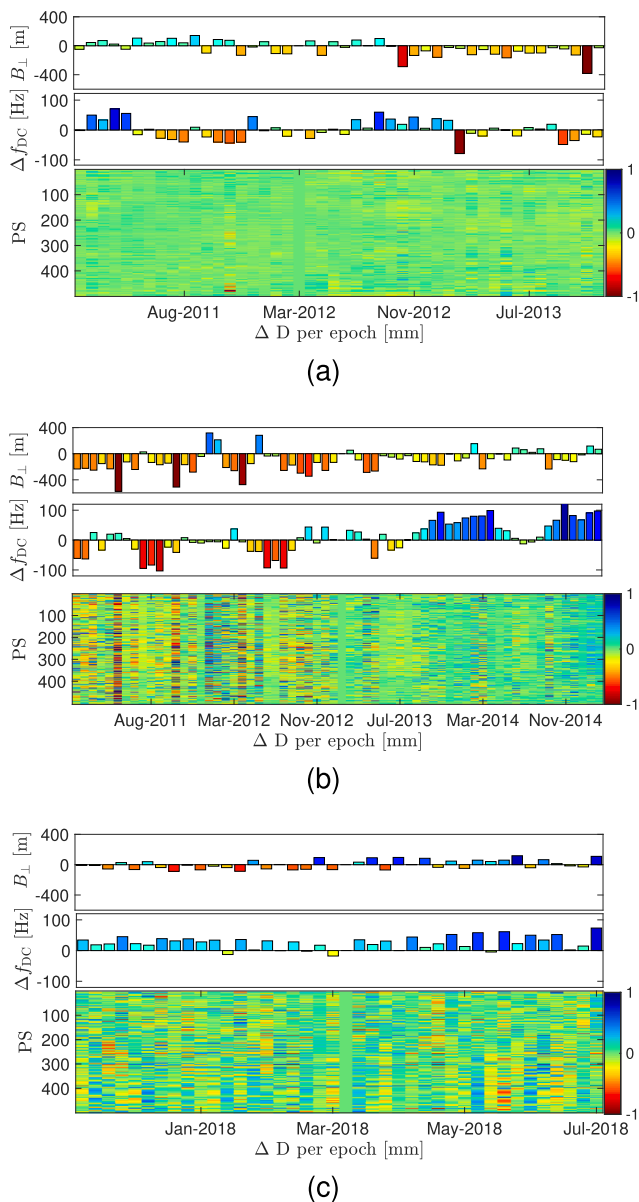

Fig. 14. The histogram of differences in the estimated velocity between SP-PSI and PSI with (a) 46 TerraSAR-X images, (b) 64 Radarsat-2 images, and (c) 40 Sentinel-1 images.

Fig. 15. Differences between PSI and SP-PSI displacements (in mm) for 500 random scatterers, as a function of time, perpendicular baselines, and Doppler centroid differences. (a) 46 TerraSAR-X images, (b) 64 Radarsat-2 images, and (c) 40 Sentinel-1 images.

Table 3
Coordinate differences (average and standard deviation) between PSI and SP-PSI [m] in the east, north, and up direction of PS with TerraSAR-X, Radarsat-2, and Sentinel-1.

	TerraSAR-X	Radarsat-2	Sentinel-1
Δe	-0.42 ± 2.55	-1.56 ± 5.56	-0.86 ± 1.57
Δn	-0.11 ± 0.65	-0.48 ± 1.44	-3.12 ± 4.14
Δu	-0.06 ± 1.18	-0.25 ± 3.92	-0.49 ± 0.59

result of 2.8 m in the east direction and for the Sentinel-1 result of about 4 m in the north direction.

Subpixel correction is essential for PSI applications where precise positioning is required, regardless of the data used. The effect of subpixel correction on deformation estimation is relatively limited and is most dominant for large orbital baselines and short time series. This
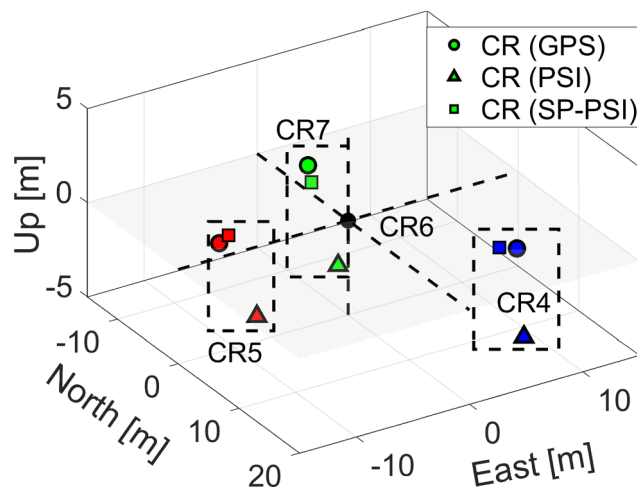
Fig. 16. Location of CR4, CR5, and CR7 relative to CR6. The circles indicate the position of CR4, CR5, CR7 estimated by GPS. The squares indicate the estimated position of the reflectors by SP-PSI with TerraSAR-X. The triangles indicate the estimated position of the reflectors by PSI.

Table 4
RMSE of double-difference coordinates by PSI and SP-PSI for TerraSAR-X with regard to GPS measurement [m].

	PSI	SP-PSI		PSI	SP-PSI
Δa	1.84	1.60	Δe	3.80	1.04
Δr	0.50	0.35	Δn	2.27	1.46
Δc	4.00	1.22	Δu	1.63	0.50

Table 5
RMSE in coordinate-differences of DBFX-CRDS in Sentinel-1 data stack by PSI and SP-PSI compared to GPS measurement [m].

	PSI	SP-PSI		PSI	SP-PSI
Δa	7.48	3.60	Δe	7.81	5.40
Δr	1.78	1.20	Δn	6.14	2.63
Δc	4.30	3.43	Δu	2.57	2.04

Table 6
Influence of sub-pixel position on PSI estimates.

	Sub-pixel position	
	Azimuth	Range
Displacement (per epoch)	No	No
Displacement velocity	iff Δf_{DC} drift	No
Height	No	Yes
Planar position	Yes	Yes

correction applies to point-like targets, whose position is well defined, which is not relevant in the case of distributed scatterers.

Declaration of Competing Interest

The authors declare that they have no known competing financial interests or personal relationships that could have appeared to influence the work reported in this paper.

Acknowledgments

Appendix A

The sub-pixel phase in range is equivalent to the reference phase variation with the incidence angle (van Leijen, 2014). The reference phase $\phi_{i,\text{ref}}$ under the far-field approximation (Hanssen, 2001) is defined as

$$\phi_{i,\text{ref}} = \frac{4\pi}{\lambda}B\sin(\theta_i^m - \alpha), \tag{A.1}$$

and therefore the variation of the reference phase as function of the incidence angle is

$$\partial\phi_{i,\text{ref}} = \frac{4\pi}{\lambda}B\cos(\theta_i^m - \alpha)\partial\theta = \frac{4\pi}{\lambda}B_\perp\partial\theta. \tag{A.2}$$

The incidence angle can be approximated by

$$\theta^m = \arccos(\frac{H_{\text{sat}}}{r_i}), \tag{A.3}$$

where H_{sat} is the height of the satellite. Thus, the incidence angle varies with slant range as

$$\partial\theta = \frac{\cos\theta_i^m}{r_i^m\sin\theta_i^m}\partial r, \tag{A.4}$$

and thus the variation of the reference phase, (A.2), can be then written as

$$\partial\phi_{i,\text{ref}} = \frac{4\pi}{\lambda}B_\perp\frac{\cos\theta_i^m}{r_i^m\sin\theta_i^m}\partial r. \tag{A.5}$$

Since, the sub-pixel phase in range is, (8),

$$\phi_{i,\eta} = \frac{4\pi}{\lambda}\cdot\frac{B_\perp}{r_i^m}\cdot\cos\theta_i^m\cdot\eta_i, \tag{A.6}$$

and the relation between η_i and the slant range is

$$\eta_i = \frac{\partial r}{\sin\theta_i^m}, \tag{A.7}$$

we conclude that the variation of the reference phase $\partial\phi_{i,\text{ref}}$ as a function of the incidence angle equals the sub-pixel phase in range $\phi_{i,\eta}$.

References

Bamler, R., Eineder, M., 2005. Accuracy of differential shift estimation by correlation and split-bandwidth interferometry for wideband and delta-k SAR systems. IEEE Geosci. Remote Sens. Lett. 2, 151–155.

Bamler, R., Schättler, B., 1993. SAR data acquisition and image formation. In: Geocoding: ERS-1 SAR Data and Systems, Wichmann-Verlag. Wichmann-Verlag, pp. 53–102.

Chang, L., Hanssen, R.F., 2016. A probabilistic approach for insar time-series post-processing. IEEE Trans. Geosci. Remote Sens. 54, 421–430.

Crosetto, M., Monserrat, O., Cuevas-González, M., Devanthéry, N., Crippa, B., 2016. Persistent scatterer interferometry: A review. ISPRS J. Photogramm. Remote Sens. 115, 78–89.

Cumming, I.G., Wong, H.C., 2005. Digital processing of synthetic radar data: algorithms and implementation. Artech House Publishers, New York.

Ferretti, A., Prati, C., Rocca, F., 2001. Permanent scatterers in SAR interferometry. IEEE Trans. Geosci. Remote Sens. 39, 8–20.

Gernhardt, S., Auer, S., Eder, K., 2015. Persistent scatterers at building facades–evaluation of appearance and localization accuracy. ISPRS J. Photogramm. Remote Sens. 100, 92–105.

Gonzalez, R.C., Woods, R.E., 2007. Digital Image Processing, third ed. .

Hanssen, R., Bamler, R., 1999. Evaluation of interpolation kernels for SAR interferometry. IEEE Trans. Geosci. Remote Sens. 37, 318–321. https://doi.org/10.1109/36.739168.

Hanssen, R.F., 2001. Radar Interferometry: Data Interpretation and Error Analysis. Kluwer Academic Publishers, Dordrecht.

Hooper, A., 2006. Persistent Scatterer Radar Interferometry for Crustal Deformation Studies and Modeling of Volcanic Deformation. Ph.D. thesis. Stanford University.

Kampes, B.M., 2006. Radar Interferometry: Persistent Scatterer Technique. Springer, Dordrecht, The Netherlands.

Keys, R., 1981. Cubic convolution interpolation for digital image processing. IEEE Trans. Acoust. Speech, Signal Process. 29, 1153–1160. https://doi.org/10.1109/TASSP.

1981.1163711.

van Leijen, F., 2014. Persistent Scatterer Interferometry based on Geodetic Estimation Theory. Netherlands Geodetic Commission, The Netherlands.

Marinkovic, P., Ketelaar, G., Hanssen, R., 2004. A controled Envisat/ERS permanent scatterer experiment, implications of corner reflector monitoring, in. In: Proceedings of the CEOS SAR Workshop.

Marinkovic, P., Ketelaar, G., van Leijen, F., Hanssen, R., 2008. InSAR quality control: Analysis of five years of corner reflector time series. In: Proceedings of the 5th International Workshop on ERS/Envisat SAR Interferometry (FRINGE '07).

Parker, J.A., Kenyon, R.V., Troxel, D.E., 1983. Comparison of interpolating methods for image resampling. IEEE Trans. Med. Imag. 2, 31–39.

Perissin, D., 2006. SAR super-resolution and characterization of urban targets. Ph.D. thesis. Politecnico di Milano. Italy.

Quegan, S., 1990. Interpolation and sampling in SAR images. IEEE Trans. Geosci. Remote Sens. 28, 641–646.

Schreier, G. (Ed.), 1993. SAR Geocoding: data and systems. Wichmann Verlag, Karlsruhe.

Shi, X., Zhang, L., Balz, T., Liao, M., 2015. Landslide deformation monitoring using point-like target offset tracking with multi-mode high-resolution terrasar-x data. ISPRS J. Photogramm. Remote Sens. 105, 128–140.

Stein, S., 1981. Algorithms for ambiguity function processing. IEEE Trans. Acoust. Speech, Signal Process. 29, 588–599.

Yang, M., López-Dekker, P., Dheenathayalan, P., Liao, M., Hanssen, R.F., 2019. On the value of corner reflectors and surface models in InSAR precise point positioning. ISPRS J. Photogramm. Remote Sens. 158, 113–122.

Zebker, H.A., Goldstein, R.M., 1986. Topographic mapping from interferometric synthetic aperture radar observations. J. Geophys. Res. 91, 4993–4999.

Zhang, H., López-Dekker, P., 2019. Persistent scatterer densification through the application of capon- and apes-based sar reprocessing algorithms. IEEE Trans. Geosci. Remote Sens. 57, 7521–7533.